AGU PUBLICATIONS

Earth and Space Science

RESEARCH ARTICLE
10.1002/2017EA000332

High Angular Resolution Measurements of the Anisotropy of Reflectance of Sea Ice and Snow

C. Goyens[1], S. Marty[2], E. Leymarie[2], D. Antoine[2,3], M. Babin[4], and S. Bélanger[1]

[1]Université du Québec à Rimouski, Département de biologie, chimie et géographie, BOREAS et Québec-Océan, Rimouski, Québec, Canada, [2]Sorbonne Universités, UPMC Univ Paris 06, INSU-CNRS, Laboratoire d'Océanographie de Villefranche, Villefranche-sur-Mer, France, [3]Remote Sensing and Satellite Research Group, Department of Physics and Astronomy, Curtin University, Perth, Western Australia, Australia, [4]Takuvik Joint International Laboratory, Québec-Océan, CNRS (France) and ULaval (Canada), Pavillon Alexandre Vachon, Département de Biologie, Université Laval, Québec, Québec, Canada

Key Points:
- Fish-eye radiance camera to measure high angular resolution hemispherical directional reflectance
- Hyperangular and spectral reflectance anisotropy of Arctic snow and sea-ice
- Directional reflectance measurements for remote sensing applications

Correspondence to:
C. Goyens,
clemgoyens@gmail.com

Citation:
Goyens, C., Marty, S., Leymarie, E., Antoine, D., Babin, M., & Bélanger, S. (2018). High angular resolution measurements of the anisotropy of reflectance of sea ice and snow. *Earth and Space Science*, *5*, 30–47. https://doi.org/10.1002/2017EA000332

Received 18 AUG 2017
Accepted 27 DEC 2017
Accepted article online 17 JAN 2018
Published online 31 JAN 2018

Abstract We introduce a new method to determine the anisotropy of reflectance of sea ice and snow at spatial scales from 1 m^2 to 80 m^2 using a multispectral circular fish-eye radiance camera (CE600). The CE600 allows measuring radiance simultaneously in all directions of a hemisphere at a 1° angular resolution. The spectral characteristics of the reflectance and its dependency on illumination conditions obtained from the camera are compared to those obtained with a hyperspectral field spectroradiometer manufactured by Analytical Spectral Device, Inc. (ASD). Results confirm the potential of the CE600, with the suggested measurement setup and data processing, to measure commensurable sea ice and snow hemispherical-directional reflectance factor, HDRF, values. Compared to the ASD, the reflectance anisotropy measured with the CE600 provides much higher resolution in terms of directional reflectance ($N = 16,020$). The hyperangular resolution allows detecting features that were overlooked using the ASD due to its limited number of measurement angles ($N = 25$). This data set of HDRF further documents variations in the anisotropy of the reflectance of snow and ice with the geometry of observation and illumination conditions and its spectral and spatial scale dependency. Finally, in order to reproduce the hyperangular CE600 reflectance measurements over the entire 400–900 nm spectral range, a regression-based method is proposed to combine the ASD and CE600 measurements. Results confirm that both instruments may be used in synergy to construct a hyperangular and hyperspectral snow and ice reflectance anisotropy data set.

Plain Language Summary In the last decades the Arctic ice pack has dramatically reduced exposing the open ocean to solar radiation. Open ocean absorbs a much larger fraction of the solar radiation than the highly reflecting ice cap. Therefore, large efforts are made to continuously measure how much solar radiation is reflected back into the atmosphere from the surface, referred to as the surface albedo. In this research a novel method has been introduced to determine the directional reflectance of sea ice and snow, a measure required to derive surface albedo from field, airborne, and satellite sensors. The method uses a multispectral fish-eye radiance camera measuring surface radiation simultaneously in all directions of a 180° field of view. Compared to directional reflectance data sets encountered in the literature, the fish-eye camera provides measurements at a much higher angular resolution and spatial resolutions more suitable for comparison with current satellite sensors (between 1 m^2 and 80 m^2). These measurements bring improvement to the interpretation of Earth-observation satellite images.

1. Introduction

The Earth-observation community often derives nadir remote sensing reflectance or albedo from directional quantities measured by off-nadir field, airborne, or satellite sensors. Therefore, the anisotropy of the reflectance of the targeted surface and overlying atmosphere needs to be considered as the directions of illumination and observation influence the measured reflectance (Nicodemus et al., 1977; Schaepman-Strub et al., 2006). Surface and atmosphere reflectance anisotropy are also of great interest for vicarious calibration of airborne and satellite sensors and atmospheric correction algorithms (Milton et al., 2009), among others, to better account for the total solar flux reflected by the area surrounding the target and diffusely transmitted to the sensor, the so-called adjacency effect (Tanre et al., 1983; Vermote & Vermuelen, 1999). This is particularly important for dark targets in bright surroundings, resulting in image blurring. Adjacency effects

are particularly acute for satellite ocean color remote sensing in polar regions, where the concurrence of bright scattering ice and dark absorbing waters generate inaccuracies that exceed the acceptable errors for providing accurate biogeochemical products (International Ocean-Colour Coordinating Group, 2016). However, the anisotropy of snow and sea ice reflectance remains difficult to simulate due to its sensitivity to a wide range of factors such as variations in atmospheric conditions, snow impurities, snow and ice state (e.g., grain size, snow, and ice morphology), vertical and horizontal heterogeneity, surface roughness, topography, and reflectance properties of the surroundings.

Here a novel method is introduced to determine the sea ice and snow anisotropy of a surface ranging from 1 m^2 to 80 m^2 at a hyperangular resolution. The new method relies on a state-of-the-art multispectral circular fish-eye radiance camera manufactured by CIMEL Electronique (Paris, France) and allows instantaneous radiance measurements over a hemisphere at about 1° and six different visible spectral bands, referred to as the CE600 (Antoine et al., 2013). In addition, reflectance anisotropy was also measured with a hyperspectral field spectroradiometer manufactured by Analytical Spectral Device, Inc. (hereafter referred to as ASD) mounted on a goniometer. The ASD measures the radiance from 350 to 1,040 nm at discrete viewing geometries and a circular or elliptical footprint varying between 49 cm^2 and 100 cm^2.

The first objective of the present study is to demonstrate the capabilities of the CE600 radiance camera to measure reflectance anisotropy, through a comparison with the ASD measurements. The second objective is to document the spectral characteristics of the reflectance anisotropy of snow and ice typically found on an Arctic landfast ice surface and its dependency on geometry of observation and illumination conditions. Finally, a method is proposed to use both instruments in synergy to construct a hyperangular and hyperspectral snow and ice reflectance anisotropy data set.

2. Background

There is a long history of reflectance anisotropy measurements, particularly over snow surfaces. Published measurements vary significantly with illumination and surface type but also in terms of angular, spectral, and spatial resolutions. Warren (1982) gives a short overview of the snow reflectance anisotropy measurements made since the late 1960s. Taylor and Stowe (1984) studied anisotropic reflectance over, among other things, snow surfaces based on satellite NIMBUS 7 Earth Radiation Budgets data with scanned surfaces ranging from 100 km^2 at nadir to 225 km^2 at horizon. Perovich (1994) measured reflectance anisotropy in the field with a 1° field of view spectroradiometer over summer snow covered ice surfaces as well as bare and ponded Arctic sea ice. The instrument was placed on a goniometer near the ground to scan small enough surfaces. These field measurements were made for a few solar zenith angles between 50° and 60°, using an angular resolution of 30° for the viewing geometry.

Near-surface spectroradiometer field measurements have also been made by Li and Zhou (2004) over snow-covered sea ice and by Bourgeois et al. (2006), Painter and Dozier (2004), and Ball et al. (2015) on different snow surfaces for a large range of solar zenith angles. Bourgeois et al. (2006) observed significant variations in snow reflectance anisotropy for solar zenith angles above 65°. Below this threshold the authors found that snow reflectance anisotropy was mainly driven by the physical characteristics of the snow layer. In addition, Bourgeois et al. (2006) and Ball et al. (2015) found that reflectance anisotropy is wavelength dependent and a function of the surface roughness. Both studies illustrate the need to provide reflectance anisotropy representative at larger spatial scales with high angular and spectral resolutions.

Measurements of reflectance anisotropy over larger snow footprints have been made in the Antarctic by Hudson et al. (2006) with a spectroradiometer placed on top of a 32 m high tower. They measured directional reflectivity for areas varying between 70 m^2 and 1,170 m^2 depending on the viewing angle in the visible and near-infrared (NIR) spectral range (400–900 nm) at 94 different solar zenith angles varying between 50° and 90°. They concluded that wavelength and solar zenith angles were sufficient to accurately parameterize the main features in snow reflectance anisotropy. Snow reflectance anisotropy measured by Hudson et al. (2006) were compared with field measurements performed by Marks et al. (2015) over the same area but with viewing footprints varying from 0.049 m^2 to 0.142 m^2. Good agreements were found between the two studies when the small scale measurements made at several sites along a 100 m transect were averaged. Reflectance anisotropy over larger sea ice and snow scenes were also estimated by Arnold et al. (2002) with a multispectral scanning radiometer, the Cloud Absorption Radiometer, mounted on the nose of a research aircraft.

At an altitude of 600 m, authors estimated a pixel resolution of 10 m at nadir and about 270 m at 80° viewing zenith angle.

Highly accurate measurements of reflectance anisotropy of snow were also carried out in the laboratory by Dumont et al. (2009). The authors measured the directional reflectance within the 500–2,600 nm spectral range for a large set of incident and viewing geometries. These measurements covered surface areas of approximately 4 cm^2 illuminated with a collimated light beam. Therefore, comparison with field measurements needs additional processing to evaluate the impact of diffuse light on the field (e.g., turbid atmospheres and significant cloud cover increasing the relative importance of diffuse light field). More recently, directional reflectance has also been measured with commercial digital cameras. For instance, Ehrlich et al. (2012) collected directional reflectivity over clouds, sea ice, and water using an airborne wide-angle lens reflex digital camera. Their measurements highlight the capability of digital cameras to instantly measure directional reflectance over an entire hemisphere without the need for high-precision movable components.

This nonexhaustive list of publications shows the wide range of measurement setups established to evaluate reflectance anisotropy over ice and snow surfaces. However, as mentioned by Ball et al. (2015), there is a need for more systematic measurements of hyperangular and hyperspectral reflectance anisotropy as well as for a larger panel of snow and ice surfaces to meet the requirements of numerous applications. In addition, there is a need in directional reflectance measurements ranging from the scale of scene individual elements to composite scenes and ultimately to airborne and satellite pixels (Milton et al., 2009). The use of wide field-of-view (FOV) cameras enables the measurement of the anisotropy of the reflectance at multiple reflectance angles simultaneously and over a large range of spatial scales without the need of additional devices (e.g., towers or airborne platforms) and high-precision goniometers. A few studies already showed the performance of wide FOV cameras for the retrieval of surface directional reflectance. Dymond and Trotter (1997) measured directional reflectance from a helicopter at 20 and 40 m from a grass field and forest canopy, respectively, with a wide-angle camera sensor. Over composite scenes, for example, forest canopy, authors suggested the use of a median composite of several images taken along a transect. Indeed, small-scale spatial inhomogeneities may erroneously be interpreted as variations in directional reflectance. By taking a median composite of several images of the composite scene, these spatial irregularities are averaged out. For a homogeneous grass field, the authors considered that a single image was sufficient to accurately estimate the directional reflectance. To further remove local variations induced by small shadows and random spatial inhomogeneity, Dymond and Trotter (1997) also applied a low-pass filter and fitted a local regression surface on the resulting directional reflectance images.

Nandy et al. (1998) developed, in support of NASA's Earth Observing System program for the vicarious calibration of satellite sensors, an imaging radiometer based on a two-dimensional charge-coupled device (CCD) array and 8 mm fish-eye lens. They observed a good agreement between the directional reflectance measurements made over desert areas with their camera and with a conventional nonimaging radiometer. (Nandy et al., 2001) further discussed the effect of calibration errors in the camera system. Based on several experiments, the authors computed the gain and offset parameters of each pixel in the 2-D imaging array, the point-spread function of the optics, the degree of polarization of the system and the lens transmission. The authors concluded that the bidirectional reflectance distribution function (BRDF) data measured with the camera were accurate to better than 1% at field angles of less than 20° and 3% for angles up to 70° . In addition, comparison between data sets taken over several vicarious calibration sites and calibration tarpaulins with the camera and a goniometer-based system confirmed that the camera measurements were as accurate as the nonimaging radiometer measurements.

3. Materials and Methods

3.1. Radiance Sensors

The CE600 and ASD instruments are complementary in terms of spectral, angular, and spatial resolution. The hyperspectral ASD measures the downward irradiance and upwelling surface radiance in a single direction between 320.3 and 1,047.865 nm with a spectral resolution of 1.4238 nm. In the present study, ASD data were measured in an uncalibrated raw digital number mode and acquired with the RS^3 ASD spectral acquisition software (https://www.asdi.com/products-and-services/software/rs3) which outputs the data at 1 nm spectral resolution. Because of imperfections in the data at wavelengths below 390 and above 950 nm, we focused only on the 400–900 nm spectral range. Reflectance factors were obtained from the raw uncalibrated readings

by taking the ratio with measurements made over a Spectralon panel (see section 3.2). Since radiance and irradiance measurements were made simultaneously, radiometric calibration was not required.

For the CE600, a detailed characterization is required to get absolute values and the correspondence between the angle of observation and its position on the detector. First, an accurate relationship was established at different directions (from −90° to +90° in 5° steps and along the four main azimuthal planes equally spaced by 45°) between a collimated light beam and its projection on the complementary metal oxide semiconductor (CMOS) detector array observed though the fish eye. This relationship considers all the geometrical distortions. Then, the attenuation introduced by the optics and the variation of the solid angle (RollOff) was quantified by measuring the ratio between a constant signal from different directions (also along the four planes, from −90° to +90° in 10° steps) and at 0° from the source. Finally, an absolute radiometric calibration was performed using a a National Institute of Standards and Technology (NIST) lamp standard. This full process allows the CE600 to measure radiances in W m^{-2} sr^{-1} simultaneously in 16,020 angular directions of a hemisphere (every 2° along the viewing azimuth angle and 1° along the zenith viewing angle) at six wavelengths in the visible (406, 438, 494, 510, 560, and 628 nm). The spectral bandwidths of the camera varies between 10 and 40 nm (see Table 2 and Figure 4 in Antoine et al., 2013). A detailed description of the design and the optical and radiometric characterization of the CE600 radiance camera can be found in Antoine et al. (2013). Three spectral bands were used in the present study, that is, 438, 560, and 628 nm. To evaluate fluctuations in the downward irradiance during the CE600 measurements, downward planar irradiance was measured simultaneously with a Satlantic Ocean Color Irradiance sensor, OCR. The OCR was fully calibrated using the same standard as the CE600 radiance camera.

3.2. Definitions and Quantities

The detailed reflectance properties of a surface are generally described by the bidirectional reflectance distribution function (BRDF). The BRDF is defined by Nicodemus (1965) as the reflectance of an incident light flux from an infinitesimal narrow incoming illumination beam at one direction in the hemisphere into another direction in the hemisphere. It is written as follows:

$$\mathrm{BRDF}(\theta_v, \Delta\theta_s, \phi, \lambda) = \frac{\mathrm{d}L_r(\theta_v, \theta_s, \Delta\phi, \lambda)}{\mathrm{d}E_d(\theta_s, \Delta\phi, \lambda)} \tag{1}$$

with $\mathrm{d}L_r(\theta_v, \theta_s, \Delta\phi, \lambda)$ being the reflected radiance measured at a viewing angle θ_v and at the wavelength λ from a surface illuminated by a collimated light beam with irradiance, $\mathrm{d}E_d(\theta_s, \Delta\phi, \lambda)$, an incident angle θ_s, and an azimuth difference between the illumination and observation vertical planes $\Delta\phi$. To some extent, equation (1) describes a surface illuminated by the Sun in a black sky without scattering and therefore without diffuse light (Schaepman-Strub et al., 2006). Therefore, BRDFs cannot be directly measured in natural illumination conditions. In the field the BRDF is often approximated by hemispherical-directional quantities (Schaepman-Strub et al., 2006). The latter considers uncollimated radiation from all downward directions including the direct and diffuse components of the solar radiation. A nondimensional quantity often used for describing reflectance anisotropy is the hemispherical-directional reflectance factor (HDRF):

$$\mathrm{HDRF}(\theta_v, \theta_s, \omega_s, \Delta\phi, \lambda) = \pi \frac{L_r(\theta_v, \theta_s, \omega_s, \Delta\phi, \lambda)}{E_d(\theta_s, \omega_s, \Delta\phi, \lambda)} \tag{2}$$

with ω_s being the incident radiance cone equal to 2π in natural conditions and $L_r(\theta_v, \theta_s, \omega_s, \Delta\phi, \lambda)$ the upwelling radiance measured at a viewing angle θ_v and wavelength λ from a surface illuminated by the Sun with a zenith angle θ_s. The downward irradiance, $E_d(\theta_s, \omega_s, \phi, \lambda)$, includes here (1) the direct irradiance at angle θ_s and $\Delta\phi$ and (2) the anisotropic diffuse irradiance which is function of the atmospheric conditions and the reflectance of the surroundings and terrain topography. Even under clear-sky conditions, natural illumination is never solely direct. Hence, in order to evaluate the illumination conditions during field measurements it is important to estimate the fractional diffuse illumination flux, $df(\lambda)$:

$$df(\lambda) = \frac{E_d^{\mathrm{dif}}(\theta_s, \lambda)}{E_d(\theta_s, \lambda)} \tag{3}$$

where $E_d^{\mathrm{dif}}(\theta_s, \lambda)$ is the diffuse downward irradiance.

Field spectroradiometers having a finite field of view provide hemispherical conical reflectance quantities rather than hemispherical directional reflectance quantities. However, under the assumption that the

bidirectional reflectance factor is isotropic within the solid angle sampled by the instrument, conical and directional reflectance factors are numerically equivalent (Bourgeois et al., 2006; Painter & Dozier, 2004).

HDRF$(\theta_v, \theta_s, \omega_s, \Delta\phi, \lambda)$ estimated from an ASD and a CE600 instrument, respectively, requires different approaches. As mentioned earlier, for the CE600 setup, $E_d(\theta_s, \omega_s, \Delta\phi, \lambda)$ was measured with the OCR. For a single image taken with the CE600 camera, HDRF$(\theta_v, \theta_s, \omega_s, \Delta\phi, \lambda)$ was then estimated following equation (2). With its radiance- and irradiance-uncalibrated sensors, the ASD requires a more step by step approach. The radiance sensor was mounted on a goniometer and measured the radiance of the surface of interest at a given illumination and viewing angle. HDRF$(\theta_v, \theta_s, \omega_s, \Delta\phi, \lambda)$ was then approximated by normalizing the surface radiance by the radiance reflected by an almost perfectly diffuse Spectralon plaque under the same illumination conditions:

$$\mathrm{HDRF}(\theta_v, \theta_s, \omega_s, \Delta\phi, \lambda) = C_{\mathrm{spec}}(\lambda)\frac{L_r(\theta_v, \theta_s, \omega_s, \Delta\phi, \lambda)}{L_r^{\mathrm{spec}}(\theta_s, \omega_s, \Delta\phi, \lambda)} \tag{4}$$

where $L_r(\theta_v, \theta_s, \omega_s, \Delta\phi, \lambda)$ is the upwelling radiance measured over the targeted surface and $L_r^{\mathrm{spec}}(\theta_s, \omega_s, \Delta\phi, \lambda)$ is the radiance measured over the Lambertian grey-white Spectralon plaque. $C_{\mathrm{spec}}(\lambda)$ is a spectral correction factor to correct the Spectralon reference surface from its deviation from an ideal Lambertian reflector panel. $C_{\mathrm{spec}}(\lambda)$ was estimated before the field campaign with a calibrated multispectral radiometer from Biospherical Instrument Inc. (Compact-Optical Profiling System, COPS). Spectralon radiance and downward irradiance data were collected with the COPS radiometer simultaneously for a large range of illumination conditions and geometries and different viewing angles. $C_{\mathrm{spec}}(\lambda)$ was then estimated for each COPS spectral band (i.e., 19 bands in the 305–780 nm spectral range) as the linear regression coefficient between the irradiance data and the upwelling radiance data. Next, regression coefficients were interpolated for the entire ASD spectral range. For the Spectralon used in the present study, $C_{\mathrm{spec}}(\lambda)$ compares well with the typical reflectance values of a white Spectralon in the blue and green spectral range (0.99 and 0.98 at 400 and 500 nm, respectively), lesser in the red and NIR where our Spectralon appeared greyer than expected (0.95 and 0.93 at 650 and 780 nm, respectively).

Radiance measurements were taken over the Spectralon plaque each time at start and end of a complete measurement cycle (with a complete cycle being the reflectance anisotropy measured over a single scene for the 25 viewing geometries). For each radiance measurement, the closest Spectralon measurement in time was used. The quantities derived from equations (2) and (4) are numerically equivalent if and only if the atmospheric conditions and associated illumination field are equal for both $L_r(\theta_v, \theta_s, \omega_s, \Delta\phi, \lambda)$ and $L_r^{\mathrm{spec}}(\theta_s, \omega_s, \Delta\phi, \lambda)$ in equation (4). Therefore, surface and Spectralon radiance measurements were normalized with simultaneously collected solar irradiance data. HDRF$(\theta_v, \theta_s, \omega_s, \Delta\phi, \lambda)$ values derived from the ASD measurements were thus estimated as follows:

$$\mathrm{HDRF}(\theta_v, \theta_s, \omega_s, \Delta\phi, \lambda) = C_{\mathrm{spec}}(\lambda)\frac{L_r(\theta_v, \theta_s, \omega_s, \Delta\phi, \lambda)}{L_r^{\mathrm{spec}}(\theta_s, \omega_s, \Delta\phi, \lambda)}\frac{E_d^{\mathrm{spec}}(\theta_s, 2\pi, \lambda)}{E_d(\theta_s, 2\pi, \Delta\phi, \lambda)} \tag{5}$$

with $E_d^{\mathrm{spec}}(\theta_s, \lambda)$ being the downwelling irradiance measured with the ASD irradiance sensor simultaneously with $L_r^{\mathrm{spec}}(\theta_s, \omega_s, \lambda)$.

In the literature several methods are used to describe the extent of the anisotropy of the reflectance and the dependency of HDRF$(\theta_v, \theta_s, \omega_s, \Delta\phi, \lambda)$ to illumination and wavelength (e.g., Ball et al., 2015; Bourgeois et al., 2006; Doctor et al., 2015; Sandmeier et al., 1998). Here we used the anisotropy index, ANIX(λ), to evaluate the extent of the reflectance anisotropy over a single surface. ANIX(λ) is calculated as the ratio of the maximum to the minimum spectral reflectance factor for a single measurement cycle (Ball et al., 2015; Bourgeois et al., 2006; Sandmeier et al., 1998). For the CE600 measurements, ANIX(λ) was estimated as the ratio of the median over the 1% highest and lowest values across the entire hemisphere. This was done to avoid the introduction of noise within the ANIX(λ). The coefficient of variation, CV(λ), was also computed for each cycle. CV(λ) is the ratio of the standard deviation to the median expressed in percentage. While the former reveals the absolute extent, the latter gives an indication of the variation in HDRF$(\theta_v, \theta_s, \omega_s, \Delta\phi, \lambda)$. Second, to evaluate the wavelength dependency of reflectance anisotropy, correlations were estimated between wavelength pairs on the directional reflectance data and on the standard normal variate, SNV$(\theta_v, \theta_s, \omega_s, \Delta\phi, \lambda)$. SNV$(\theta_v, \theta_s, \omega_s, \Delta\phi, \lambda)$ is often used to apply baseline and light scattering correction (Barnes et al., 1989). Here it allowed focusing

on the shape of the spectrum rather than on its magnitude. SNV(θ_v, θ_s, ω_s, $\Delta\phi$, λ) was calculated for every spectrum individually and for each angle θ_v, θ_s and $\Delta\phi$ as follows:

$$\mathrm{SNV}(\theta_v, \theta_s, \Delta\phi, \lambda) = \frac{\mathrm{HDRF}(\theta_v, \theta_s, \omega_s, \Delta\phi, \lambda) - \mu_{\mathrm{HDRF}(\theta_v,\theta_s,\omega_s,\Delta\phi)}}{\sigma_{\mathrm{HDRF}(\theta_v,\theta_s,\omega_s,\Delta\phi)}} \quad (6)$$

where $\mu_{\mathrm{HDRF}(\theta_v,\theta_s,\omega_s,\Delta\phi)}$ is mean HDRF over the entire spectral range for a given angle θ_v, θ_s, and $\Delta\phi$ and $\sigma_{\mathrm{HDRF}(\theta_v,\theta_s,\omega_s,\Delta\phi)}$ is the standard deviation. To simplify notation, angular dependence is omitted hereafter for HDRF and SNV.

Next, the feasibility of using a regression model to reconstruct the CE600 HDRF(λ) estimations at any wavelength in the 400–900 nm spectral range was evaluated. To do this, a regression model was used to simulate CE600 HDRF(λ) in the red spectral region using CE600 HDRF(λ) measurements in the blue and green spectral range. Modeled HDRF values were estimated as follows:

$$\mathrm{HDRF}_{\mathrm{RR}}(628) = C_{438}\mathrm{HDRF}(438) + C_{560}\mathrm{HDRF}(560) \quad (7)$$

where HDRF(438) and HDRF(560) are the CE600 measured HDRF data and $\mathrm{HDRF}_{\mathrm{RR}}(628)$ is the regression based HDRF in the red spectral range. C_{438} and C_{560} are the regression coefficients estimated using the hyperspectral ASD data. The performance of the regression method was evaluated based on the percentage relative error (RE) between the modeled and measured HDRF as follows:

$$\mathrm{RE} = 100\frac{\mathrm{HDRF}_{\mathrm{RR}}(628) - \mathrm{HDRF}(628)}{\mathrm{HDRF}(628)} \quad (8)$$

3.3. Measurement Setup and Data Processing

Directional reflectance measurements over bare ice, snow, and ponded ice surfaces were carried out during a field experiment between 23 May and 7 June 2015 in the frame of the GreenEdge project. Data were collected in southern Baffin Bay, Nunavut, at two different locations on the landfast first-year ice: (1) near the Inuit village of Qikiqtarjuak (64.03°N, 67.56°W) and (2) at the GreenEdge 2015 ice camp 23 km from the village (67.47°N, 63.79°W).

In addition to field notes describing illumination and surface conditions, a MICROTOPS II five-channel hand-held Sunphotometer was used to measure water vapor and aerosol optical depth as often as possible during the radiance measurements. A meteorological station was also present at the ice camp, measuring temperature, relative humidity, and wind speed data continuously. Here the meteorological and MICROTOPS data were used as inputs in the spectral solar irradiance model of Gregg and Carder (1990) to estimate $df(\lambda)$. When no MICROTOPS and meteorological measurements were available, an optimization method was used to evaluate direct and diffuse solar illumination based on the field measured total irradiance. The optimization method consisted of minimizing the difference between field and simulated total irradiance by varying the visibility within the model. The optimization uses relative humidity, wind speed, date, time, latitude, and longitude as inputs and considers the default values suggested by Gregg and Carder (1990) for atmospheric water vapor content. Differences between optimization-based and estimated $df(\lambda)$ did not exceed 10% confirming the robustness of the optimization method.

Other data measured in the frame of the GreenEge project were also made available, such as sea ice thickness and snow depth, which were measured at several points on the ice camp. Snow properties, including snow specific surface area, were also measured every 2 days. Snow radii were subsequently estimated from snow specific area values (Gallet et al., 2014).

Figure 1 shows the measurement setup in the field for the ASD and CE600 sensors. At nadir, the footprint of the ASD corresponds to a circular area with a diameter of 7 cm. At 60° viewing zenith angle the footprint gets ellipsoidal with minor and major axes of about 7 and 15 cm, respectively. Radiance measurements with the ASD sensor were made every 30° in azimuth from 0° to 360° and at zenith angles of 0°, 30°, and 60° yielding 25 hyperspectral reflectance measurements for a given surface. Note that the term "forward reflection" is used here to design the photon reflected between +90° and −90° of azimuth relative to the Sun positioned at 180° (i.e., the same direction as the specular reflection).

The ASD irradiance sensor was mounted on a tripod at a height of 1.2 m and some distance from the goniometer to avoid shading when operating the instrument. A full cycle (i.e., 25 radiance measurements over the snow or ice surface and 2 Spectralon measurements) lasted approximately 30 min.

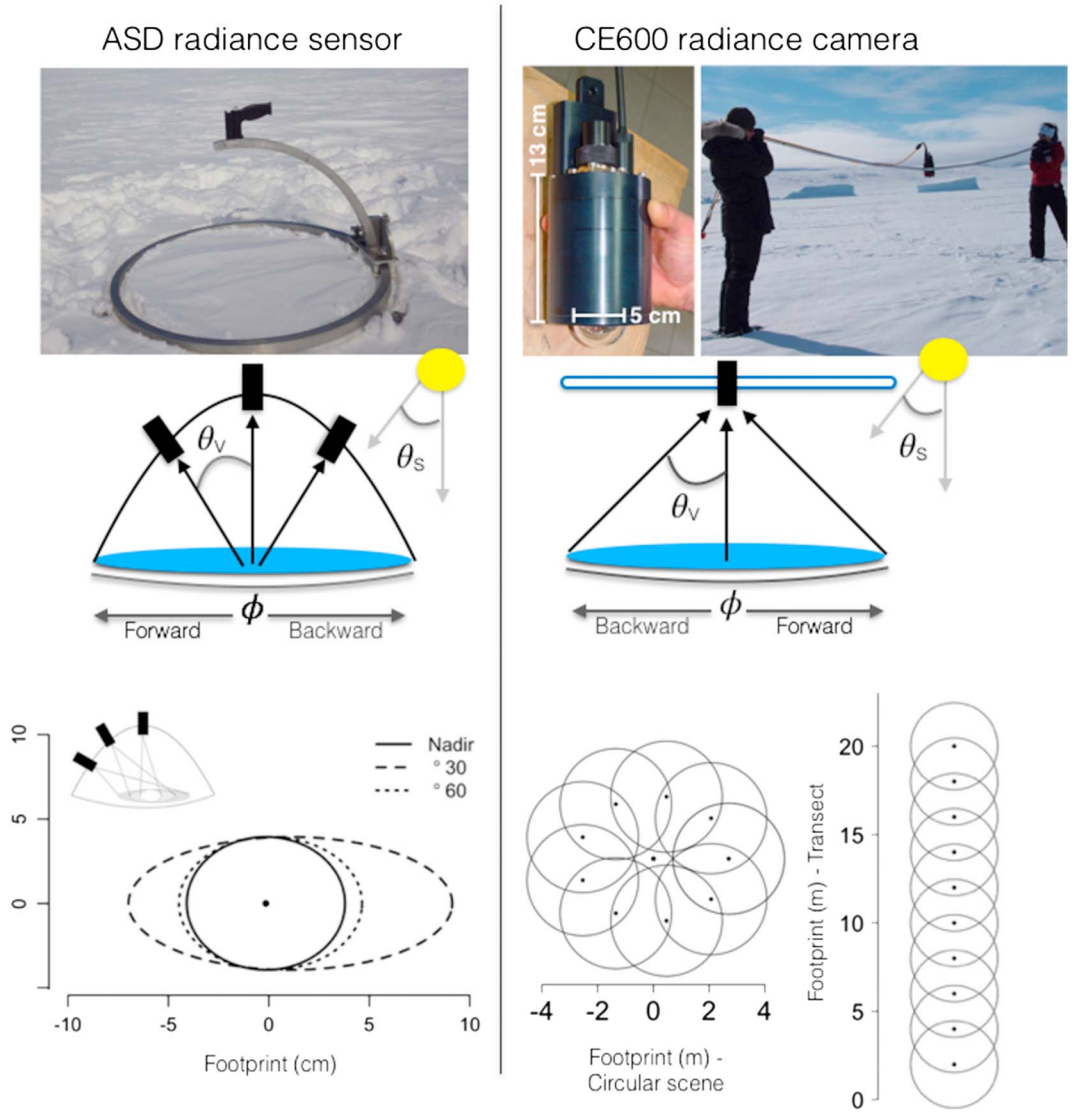

Figure 1. Pictures and schematic representation of the field setup to measure reflectance anisotropy with the ASD and CE600, respectively, and the footprint of the surfaces scanned with the two instruments according to their setup.

CE600 measurements were taken successively with the ASD measurements along a 10 to 20 m long transect or over a circular footprint with a surface varying between 1 and 8 m (Figure 1). CE600 measurements were made close to the ASD measurements to ensure similar surface types. Caution was also used such that CE600 measurements were made over homogeneous surfaces of snow, ice, and ponded ice such that each CE600 station could be described by a single surface type.

According to the height of the instrument and the distance of the transect or the diameter of the circular footprint, the surface scanned for the computation of the CE600 directional reflectance varied from 1 m^2 to 80 m^2. The CE600 fish eye was mounted in the middle of a 4.20 m long pole (Figure 1) and took an hemispherical image with viewing zenith angles along the camera axis from 0° to 90°. Here we excluded any viewing angle above 60°. Accordingly, when the pole was held at approximately 1.2 m from the ground, each individual CE600 image covered an circular area with a diameter of approximately 4.15 m and each pixel within the CE600 images represented the surface radiance for a given angle θ_v and $\Delta\phi$ (Figure 1). Several images were taken over a single surface type (referred to as station) along a 10 to 20 m transect or over a circular footprint of 2 to 10 m^2. Images with more than 500 saturated pixels or with a camera tilt exceeding 5° were excluded, resulting in about 20 to 150 images per station and per wavelength. For each retained image, camera counts were then converted to radiance measurements following the procedure detailed by Antoine et al. (2013).

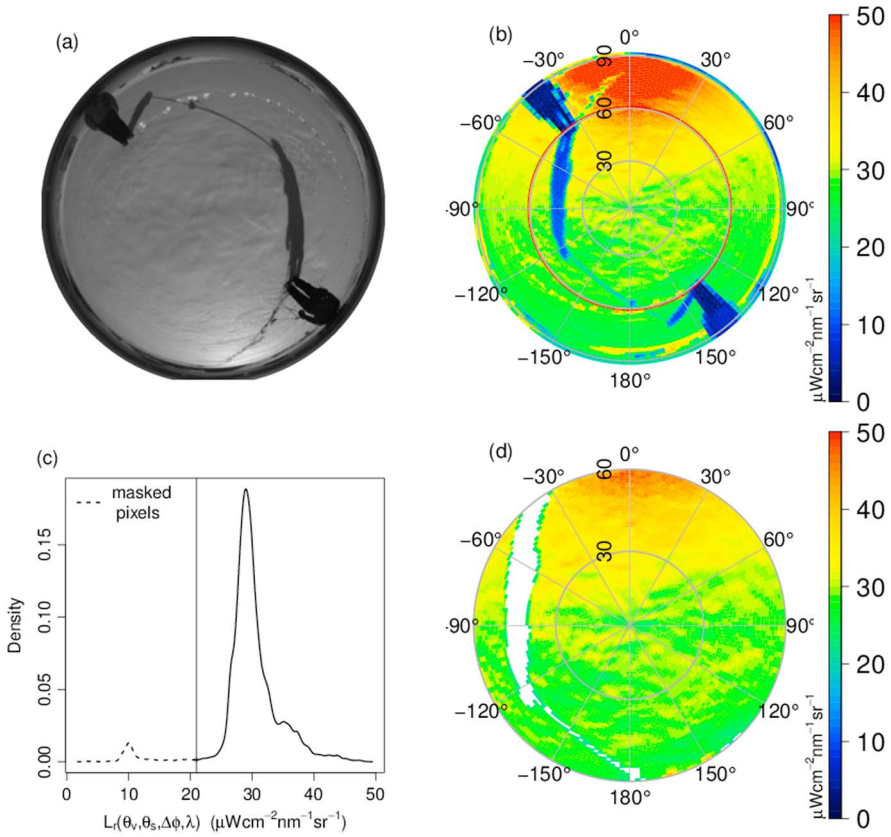

Figure 2. Example of CE600 data processing for a single image taken over a snow surface: (a) raw CE600 image, (b) $L_r(\theta_v, \theta_s, \Delta\phi, \lambda)$ after Sun azimuth detection, (c) frequency distribution function used to eliminate shadow contaminated pixels, and (d) $L_r(\theta_v, \theta_s, \Delta\phi, \lambda)$ cropped at 60° viewing zenith angle after the removal of contaminated pixels by the shadow (white pixels = no data).

Next, we developed a method to evaluate the Sun azimuth in each hemispherical image. The method relied on three assumptions: (1) the Sun is the most reflective object within the CE600 images around 90° zenith viewing angle, (2) sea ice and snow surfaces are strongly forward reflecting surfaces, and (3) shadow from camera holders or the instrument itself should be in the opposite direction of the sun azimuth.

Finally, a method was developed to remove artifacts within the images (e.g., shadows, snow packs on bare ice surface, or other high reflective objects). The method was based on a frequency histogram of the radiance within each image. If a frequency distribution is bimodal, it was assumed that the mode with the lowest amplitude is associated with either shadow or highly reflective objects. Any pixel showing values outside the principal mode were therefore removed from further data analysis. Figure 2 illustrates the image processing of a typical snow image. It shows the raw CE600 image (Figure 2a), a radiance polar plot after it has been rotated to force the forward reflection to be between −90° and 90° (Figure 2b), the frequency distribution function used to eliminate shadow contamination (Figure 2c), and the image cropped at 60° zenith viewing angle (Figure 2d). To estimate HDRF(λ) for a single image, the radiance in each pixel was divided by the irradiance measured simultaneously with the multispectral reference OCR sensor. OCR irradiance measurements were interpolated to the CE600 wavelengths according to the model of Gregg and Carder (1990), taking into account the spectral response function of the instrument. Finally, a median composite was computed per wavelength from all the reflectance images taken at a single station (i.e., from 20 to 150 images). This allowed us to eliminate small irregularities and to obtain directional reflectance data representative of areas ranging from 2 to 80 m^2 spatial resolutions. Each station was thus associated with a matrix of median HDRF(λ) along θ_v and $\Delta\phi$ and a matrix of the coefficient of variation, $CV_{pixels}(\lambda, \theta_v, \Delta\phi)$, to evaluate the variation in HDRF(λ) for each pixel within the image.

From the resulting median HDRF(λ) composite, the parameters ANIX(λ) and CV(λ) were estimated for each image as described in section 3.2.

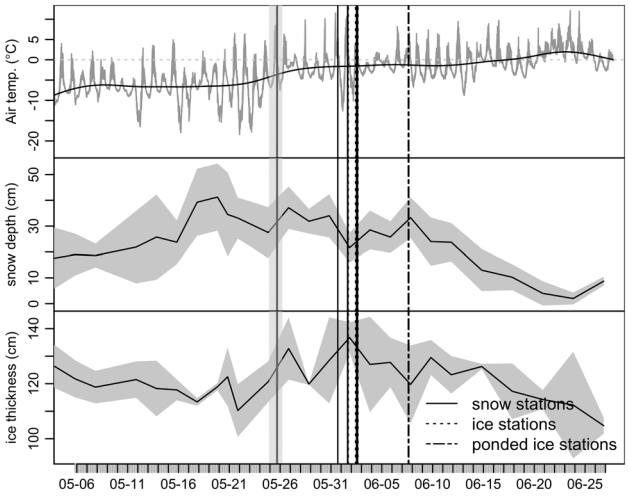

Figure 3. Temporal evolution of the air temperature (°C), the snow depth (cm), and ice thickness (cm) at the GreenEdge ice camp 2015 during the HDRF(λ) measurements. Solid, dotted, and dashed lines correspond to the dates of the HDRF measurements detailed in the present study and taken over snow, ice, and ponded ice surfaces, respectively. The semitransparent light grey bar corresponds to 25 May, the date the mean daily air temperature first reached 0°C.

4. Results and Discussion

4.1. Measurement Sites, Snow, and Ice Surface Properties

The field experiment was conducted on first-year ice and coincided with the transition period between the onset of melting and pond formation. In 2015, exceptionally thick snow cover was recorded during the spring (Figure 3), thus explaining why the timing between melt and pond onsets was longer than normal (Yackel et al., 2007). Overall, the average air temperature increased during the field experiment from 25 May to 6 June. The mean daily air temperature also first reached 0°C on 25 May. At the beginning of the field experiment, rapid variations in sky conditions (alternation of clear sky and diffuse cloud cover) and air temperatures (above and below freezing point) were observed, resulting in noticeable diurnal variations in the snow surface (Figures 4a–4c). Snowing events were also recorded on 26 and 28 May. Snow grain radii varied between 0.1 and 0.4 mm which, according to the definitions of Grenfell and Perovich (2004), correspond to cold snow (Figure 4a) and the beginning of melting snow (Figure 4b), respectively. Between 1 June and 2 June, a substantial cooling event occurred during the night, thus explaining the glazed snow surface observed the morning of 2 June (Figure 4c). With solar heating, the glazed snow surface melted rapidly in the afternoon. Meanwhile, scientific operations being conducted as part of our experiment, including the cleaning of snow cover, accelerated the melting of the snow pack over several ice surfaces at the GreenEdge ice camp. These surfaces covered an area of approximately 10 m^2. On 1 June, HDRF measurements were made over these sea ice surfaces presenting a thin (<2 cm) surface scattering layer. This surface scattering layer showed distinctive diurnal patterns. In the morning we noticed a granular texture and the presence of highly reflective ice grains (Figure 4d), while in the afternoon the ice grains melted to a consolidated wet upper ice layer (Figure 4e). On 6 June, with the increasing average temperature,

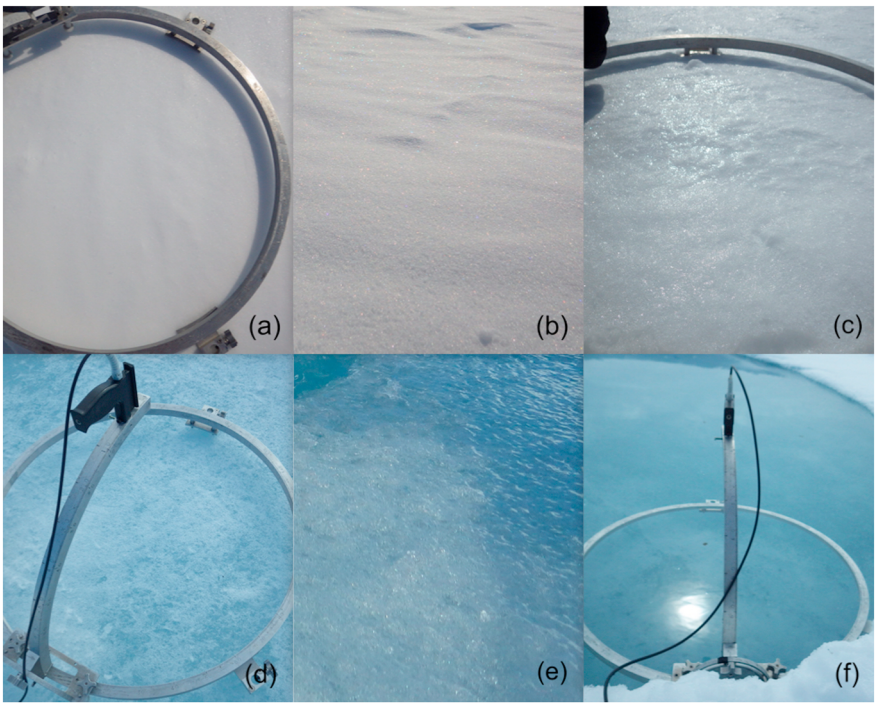

Figure 4. Pictures taken at ASD and CE600 stations over (a) cold, (b) melting, and (c) glazed snow surfaces, over snow-free ice with a (d) granular and (e) melted scattering layer, (f) and over ponded ice.

Table 1
Station Name ([Instrument][θ_s][Surface Type]) and, for the CE600 Stations Only, the Surface Scanned to Compute the Directional Reflectance ((Between Brackets in m^2), Date and Time (Local Time, UT−4H), Solar Zenith Angle (θ_s), Surface Description (Surf), Cloud Cover and Average Wind Speed (W), Temperature (T), Relative Humidity (RH), and Fraction of Diffuse Light at 438, 560, and 628 nm (df (λ))

	Date and local time	θ_s (deg)	Surf	Cloud cover	W (m/s)	T (°C)	RH (%)	df(438) (%)	df(560) (%)	df(628) (%)
ASD58snow	2015-05-25 at 15:57	58.02	Cold snow	Variable	1	−0.42	63	29	13	10
ASD67snow	2015-05-25 at 17:36	67.20	Melting snow	Variable	1	0.52	60	37	18	13
CE60064snow (43.6)	2015-05-25 at 16:55	63.56	Melting snow	Variable	1	0.11	63	42	25	19
ASD46snow	2015-05-31 at 16:06	45.63	Melting snow	Clear	2	1.10	72	34	18	14
ASD53snow	2015-06-01 at 15:05	52.66	Melting snow	Clear	2	3.12	55	26	13	9
CE60056snow (83.1)	2015-06-01 at 15:47	56.32	Cold snow	Clear	2	2.97	50	36	21	16
CE60057snow (54.3)	2015-06-01 at 15:57	57.19	Cold snow	Clear	2	2.71	49	36	21	16
ASD45snow	2015-06-02 at 12:11	45.44	Glazed snow	Clear	5	−0.01	66	22	12	9
ASD52snow	2015-06-02 at 14:54	51.93	Glazed snow	Variable	5	0.33	66	26	15	12
CE60059ice (9.6)	2015-06-01 at 16:18	59.11	Bare ice	Clear	2	1.62	55	38	22	17
CE60060ice (9.6)	2015-06-01 at 16:23	59.52	Bare ice	Clear	2	1.89	51	38	22	17
ASD63ice	2015-06-01 at 16:52	62.99	Bare ice	Clear	2	1.04	56	33	16	12
ASD50ice	2015-06-02 at 10:04	49.62	Bare ice	Clear	3	−0.89	66	25	14	11
CE60047ice (2)	2015-06-02 at 11:06	46.6	Bare ice	Clear	3	1.13	60	25	14	11
CE60046ice (2)	2015-06-02 at 11:36	45.79	Bare ice	Clear	3	1.14	60	24	14	11
CE60045ice (2)	2015-06-02 at 12:06	45.45	Bare ice	Clear	3	0.56	62	22	11	9
CE60051ice (2)	2015-06-02 at 14:43	51.12	Bare ice	Variable	5	0.16	68	26	15	12
CE60053ice (2)	2015-06-02 at 15:06	52.85	Bare ice	Variable	5	0.36	67	27	15	12
CE60056ice (2)	2015-06-02 at 15:47	56.17	Bare ice	Variable	4	0.02	68	29	16	13
ASD50meltpond	2015-06-07 at 18:31	49.52	Ponded ice	Variable	2	1.69	71	27	14	10
CE60056meltpond (2)	2015-06-07 at 19:53	56.08	Ponded ice	Variable	2	1.30	73	31	16	12

Note. Dates are formatted as yyyy-mm-dd.

the depressed snow-free ice surface produced the first melt pond at the GreenEdge ice camp, filled with a layer of approximately 11 cm melt water and surrounded by a snow-covered ice layer (Figure 4f).

Table 1 summarizes the data measured with both the ASD (9 stations) and CE600 (12 stations) for the three surface types (snow, bare ice, and ponded ice), the simultaneously measured meteorological data, and the estimated $df(\lambda)$. The surfaces scanned by the CE600 instrument varied from 2 m^2 to 83 m^2 (Table 1). Directional reflectance for stations CE60064snow and CE60056snow are a median composite of images taken over a transect covering a surface of about 42 and 83 m^2, respectively. Directional reflectance at station CE60057snow was computed for a circular footprint with an area of 54 m^2. Over the ice stations, the directional reflectance was estimated for circular surfaces varying from 2 to 9.2 m^2.

4.2. Reflectance Anisotropy Measurements

Figure 5 shows the HDRF(λ) measured with the ASD for snow, bare ice, and ponded ice. All measurements were performed with solar zenith angles around 50° under clear sky with diffuse light contribution ($df(\lambda)$) around 25%, 15%, and 10% at 438, 560, and 628 nm, respectively. HDRF(λ) values over snow surfaces remain close to 1 with maximum and minimum values of around 1.15 and 0.9, respectively. Over the bare ice surfaces HDRF(λ) values were lower with a maximum of 0.75 and a minimum of 0.4. For ponded ice surfaces HDRF(λ) values did not exceed 0.55 with a minimum near nadir and a maximum in the direction of the solar beam specular reflection.

Figure 6 shows CE600 median HDRF(λ) values and Figure 7 the $CV_{pixels}(\lambda, \theta_s, \Delta\phi)$ at 438, 560, and 628 nm, for measurements made along the ASD measurements shown in Figure 5. The time lapse between the ASD and CE600 measurements did not exceed 1 h.

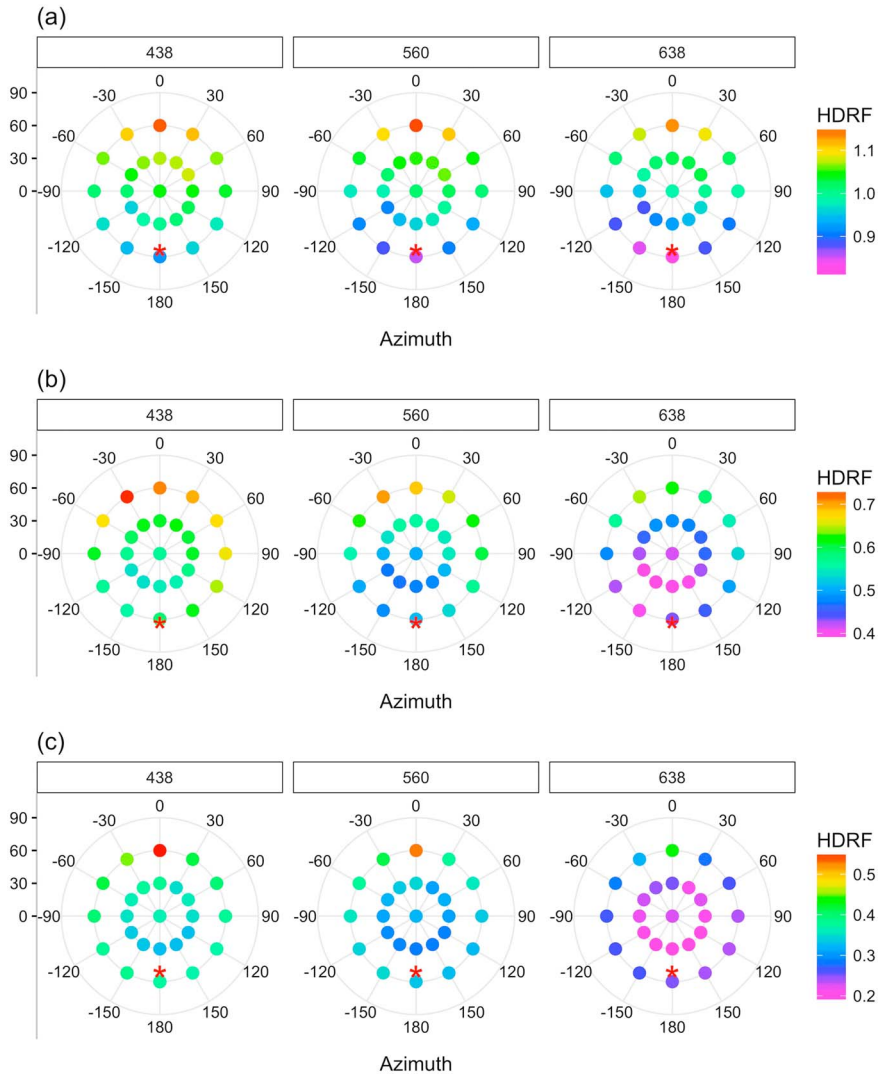

Figure 5. Polar plots of HDRF(λ) measured with the ASD for three different surfaces, snow (a, ASD53snow), bare ice (b, ASD63ice), and ponded ice (c, ASD50meltpond) at 438, 560, and 628 nm. The Sun (red cross) is at $\Delta\phi = 180°$ and forward reflection in the upper hemisphere ($\Delta\phi$ between $-90°$ and $\Delta\phi = 90°$).

Figures 6a–6c correspond to the median composite of 42 to 46 images. The number of images varies according to the wavelength. Images were taken along a transect of approximately 10.5 m under a clear sunny sky. The $CV_{pixels}(\lambda, \theta_s, \Delta\phi)$ values in Figures 7a–7c did not exceed 10%, suggesting a relatively smooth and homogeneous snow surface. HDRF(λ) measurements taken over similar snow surfaces and under identical illumination conditions but based on different setups, namely, circular versus linear (cf. Figure 1), are qualitatively and quantitatively comparable (not shown here). This confirms that both setups are appropriate for measuring surface reflectance anisotropy with the CE600.

The bare ice station shown in Figures 6d–6f corresponds to a flat grey-bluish ice surface with a thin surface scattering layer of coarse ice grains. The median HDRF(λ), measured with a θ_s of 60°, is the median composite of 20 to 26 radiance images taken over a circular area of 4 m in diameter. The HDRF(λ) ranged from 0.37 to 1.50. $CV_{pixels}(\lambda, \theta_s, \Delta\phi)$ values for the bare ice surfaces are slightly higher compared to the snow surfaces (Figures 7a–7c versus Figures 7d–7f), particularly between 0° and 90° $\Delta\phi$. These higher values of $CV_{pixels}(\lambda, \theta_s, \Delta\phi)$ are explained by the presence of thawed ice nearby highly reflective ice grains. This is often observed at the beginning of the melt season when freeze-thaw cycles occur at the snow-air interface. As mentioned earlier, measurements over bare ice were limited to sea ice surfaces cleaned from their snow cover.

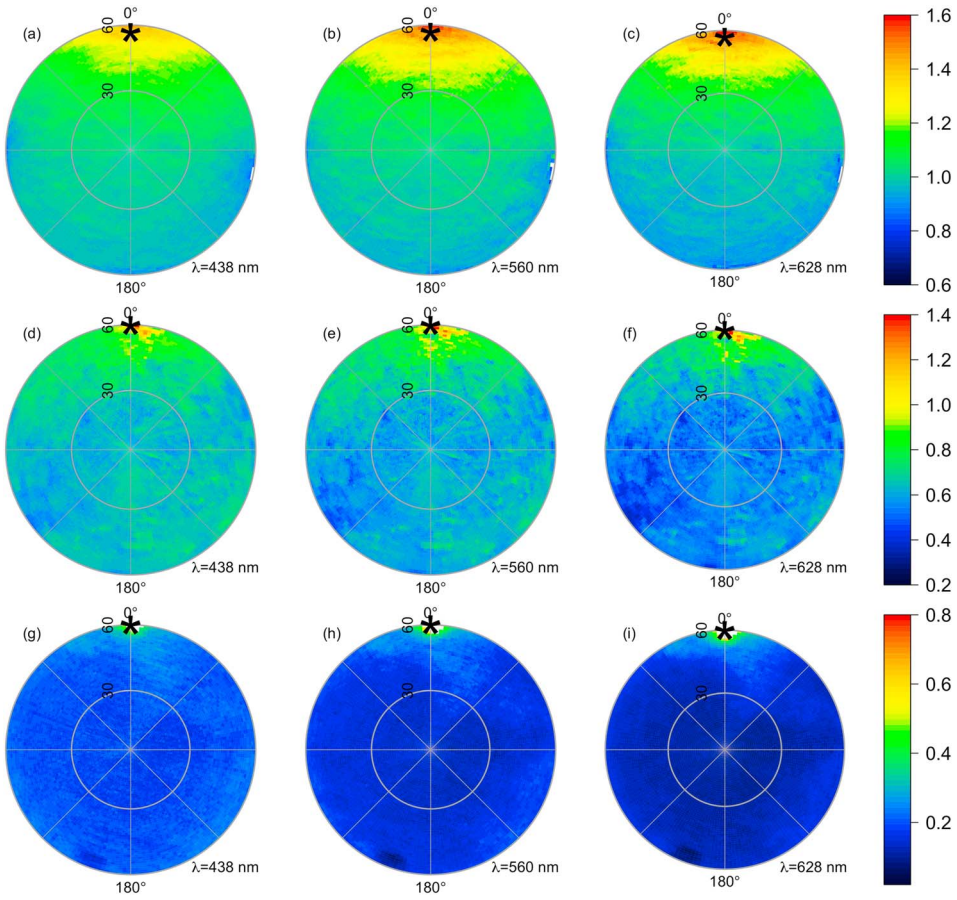

Figure 6. Polar plots of median HDRF(λ) measured with the CE600 for three different surfaces, snow (a–c, CE60056snow), bare ice (d–f, CE60060ice), and ponded ice (g–i, CE60056meltpond) at 438, 560, and 628 nm. Forward reflection is in the upper hemisphere (from $\Delta\phi = -90°$ to $\Delta\phi = 90°$) and the black star indicates the sun position in each plot.

Measurements were thus made over relatively small areas (about 10 m^2), and some spatial inhomogeneities could not be avoided. By taking a median HDRF(λ) over several images of the area, these local variations were, however, removed.

Figures 6g–6i show the median HDRF(λ) images for a dark ponded ice surface. For the three bands, the median is estimated over 50 images. The HDRF(λ) ranges from 0.13 to more than 2. These very high values are the result of the specular reflection of the sun at the air-water interface of the water pond (see Figure 4). The ponded ice surface also shows higher $CV_{pixels}(\lambda, \theta_s, \Delta\phi)$ values compared to bare ice and snow surfaces in particular in the blue and green spectral region (Figures 7g–7i). This higher degree of variation is partially explained by inaccuracies in the data processing to remove artifacts and shadow within the image. Indeed, the reflectance properties of shadow in these spectral bands are similar to the reflectance properties of the ponded ice surface making it difficult to eliminate shadow contamination within the image. However, as for Figures 7d–7f, these inaccuracies in data processing and surface irregularities are averaged out when taking a median composite but remain, however, associated to higher $CV_{pixels}(\lambda, \theta_s, \Delta\phi)$ values.

Figure 8a shows the HDRF(λ) taken at nadir for all stations detailed in Table 1. As expected, lower reflectance factors are measured over bare ice and melt ponds, while more reflective reflectance spectra are measured over snow surfaces. For comparison, the nadir spectra measured by Perovich (1994) over a snow and glazed snow surface, over a blue and bare ice surface, and over a ponded ice surface are added in Figure 8a. Measurements reported by Perovich (1994) coincide well with both the ASD and CE600 measurements for the three surface types. The nadir HDRF(λ) data in Figure 8a are also in agreement with the albedo measurements made by Grenfell and Perovich (2004) over first-year ice near Barrow in Alaska (see Figure 10 in Grenfell & Perovich, 2004). The authors measured the average albedo with an ASD over snow, ice, and ponded ice along 200 m long transects. Our nadir HDRF(λ) measurements made over snow surfaces fall in between

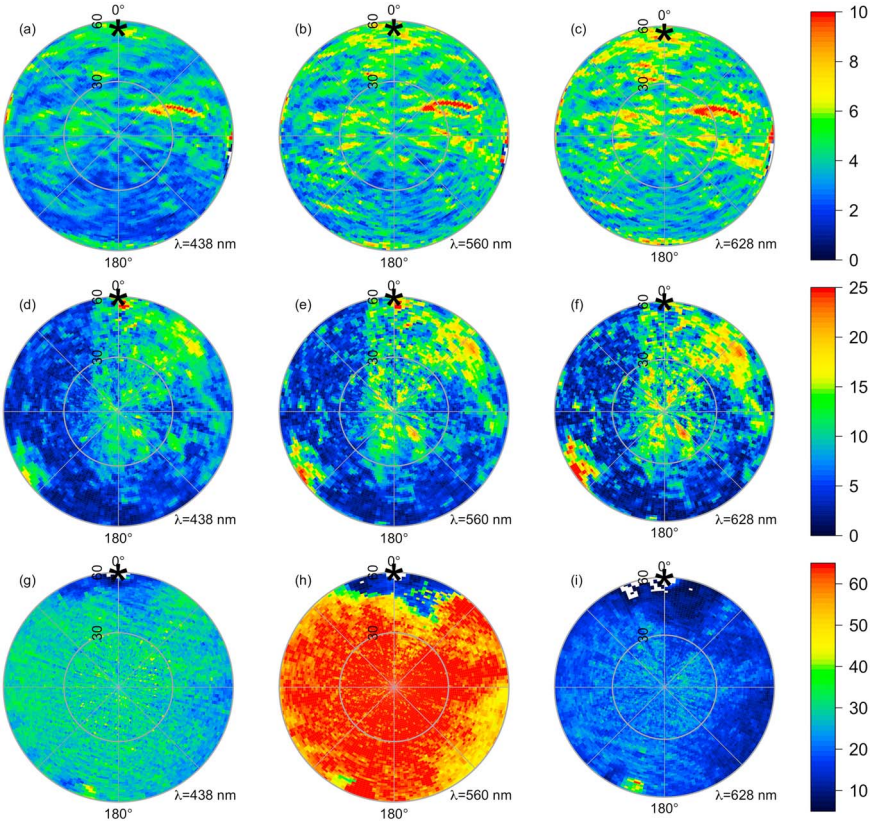

Figure 7. Same as in Figure 6 but for the $CV_{pixels}(\lambda, \theta_s, \Delta\phi)$ estimated together with the median HDRF(λ).

the cold and melting snow albedos measured by Grenfell and Perovich (2004). The most reflective HDRF(λ) ice spectrum corresponds to the deteriorated ice albedo of Grenfell and Perovich (2004), while the less reflective HDRF(λ) ice spectrum corresponds to the undeteriorated and blue-green ice albedos. The surface metamorphism from deteriorated to undeteriorated melting ice was also observed in the field when the directional reflectance was measured over a same ice layer during an entire day (i.e., on 2 June in Table 1). The highly reflective granular surface scattering layer (Figure 4d) observed in the morning melted with the solar heating to form a less reflective surface scattering layer (Figure 4e). Finally, the nadir HDRF(λ) measurements taken over ponded ice are consistent with the early meltpond spectra measured by Grenfell and Perovich (2004).

According to Figure 8b, the anisotropy of the reflectance decreases with increasing albedo and varies according to the snow properties and melting stage. Over snow surfaces, ANIX(λ) are relatively constant ranging between 1 and 2 in the visible and NIR spectral bands (Figure 8b). Cold snow with smaller snow grain radii ($\sim$0.1 mm) approaches a Lambertian behavior (ANIX(λ)$\sim$1), while larger granular grains and glazed snow show more variability in directional reflectance (ANIX(λ) $>$ 1).

For bare ice surfaces, ANIX(λ) increases with wavelength and when the ice surface is melting with a maximum value around 3. For most stations, CE600 data show higher ANIX(λ) values compared to the ASD data. This is explained by the angular resolution of the camera that better depicts the minima and maxima in HDRF(λ). For the same reason, the sharp increases in HDRF(560) at $\Delta\phi$ equals 0° and θ_s equals 60° in Figures 8c and 8d, respectively, are more pronounced with the CE600 data. This is particularly true for the bare ice surfaces where the peak in reflectance anisotropy in the direction of the solar beam is often sharper. In addition, a darkening of HDRF(λ) along the grazing angles is also observed with the CE600 and not with the ASD (Figure 8c).

Overall, for a same surface type, nadir HDRF(λ) data measured with the ASD tend to be more variable than the nadir HDRF(λ) measured with the CE600. In addition, according to Figures 8a, 8c and 8d, the CE600 directional reflectance data tend to be higher compared to the ASD measurements. These differences may be explained by several factors: (1) smaller footprints (i.e., with the ASD) are expected to be more affected by small-scale

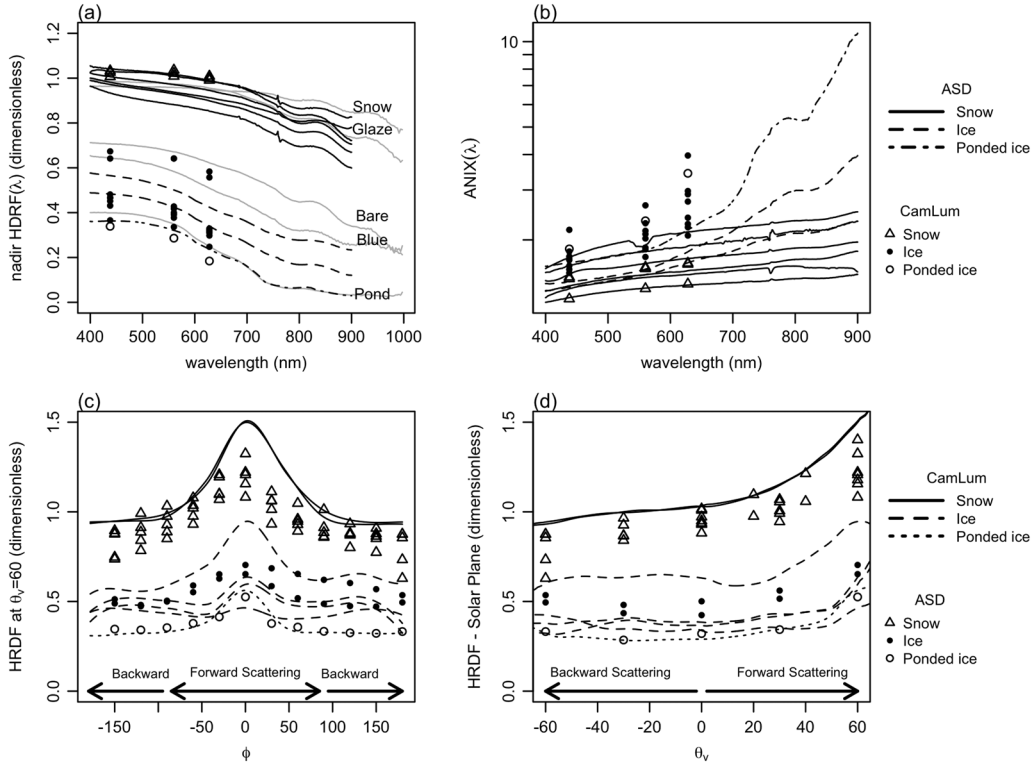

Figure 8. Nadir (a) HDRF(λ) and (b) ANIX(λ) measured with the CE600 (points) and the ASD (lines) for the stations described in Table 1 and HDRF(560) measured at (c) $\theta_v = 60°$ and in the (d) solar plane with the CE600 (lines) and the ASD (symbols). For comparison, nadir HDRF(λ) measured by Perovich (1994) are added in Figure 8a (light grey solid line).

heterogeneities (e.g., grain size and small-scale surface inhomogeneities) resulting in a higher degree of variability over a same surface type, (2) with the CE600 sensor, the radiance is measured at a higher height and is therefore slightly affected by diffuse illumination and subsequent adjacency effect, and (3) small differences in HDRF(λ) may result from differences in θ_s and subsequent changes in illumination (e.g., cloud cover affecting the fractional diffuse sunlight) as well as surface metamorphism (due to heating, cooling and variations in wind and/or relative humidity).

4.3. Variations in Reflectance Anisotropy with Illumination Conditions

Snow ANIX(λ) remains approximately constant with θ_s for both the ASD and CE600 instruments ranging between 45° and 67° (not shown here). Similarly, for snow surfaces no significant relationship was observed between CV(λ) and θ_s (not shown here). This is in agreement with Bourgeois et al. (2006) who observed that the direct relationship between ANIX(λ) and θ_s is only significant for θ_s values greater than 65°. On the contrary, over bare ice surfaces ANIX(λ) varies more significantly with illumination conditions. As shown in Figure 9a, ANIX(λ) tends to decrease with increasing θ_s. This inverse relationship is even more pronounced between CV(λ) and θ_s and between CV(λ) and $df(\lambda)$ (Figures 9b and 9c). This is observed with both the ASD and CE600 measurements. Hence, a detailed description of the illumination conditions is required when measuring reflectance anisotropy in the field. Discarding important information such as θ_s, $df(\lambda)$ and relative humidity may render intercomparison of results across studies very difficult. Note, however, that θ_s and $df(\lambda)$ are correlated since direct and diffuse irradiance are proportional to the cosine of θ_s (e.g., see in Gregg & Carder, 1990). This is particularly true under clear-sky conditions. Here we calculated correlation coefficients (r^2) from 0.89 to 0.92 between θ_s and $df(443)$. Though under more turbid atmospheres, r^2 is expected to decrease and $df(\lambda)$ and θ_s are expected to inversely impact reflectance anisotropy.

4.4. Variations in Reflectance Anisotropy With Wavelength

Wavelength dependency of reflectance anisotropy over snow and ice surfaces has already been documented. Most studies reported that in the visible and NIR spectral region, wavelength dependency is explained by (1) the increasing surface absorption with wavelength caused by variations in the snow or ice properties and the presence of impurities in the snowpack and/or (2) the decreasing Rayleigh scattering and subsequent

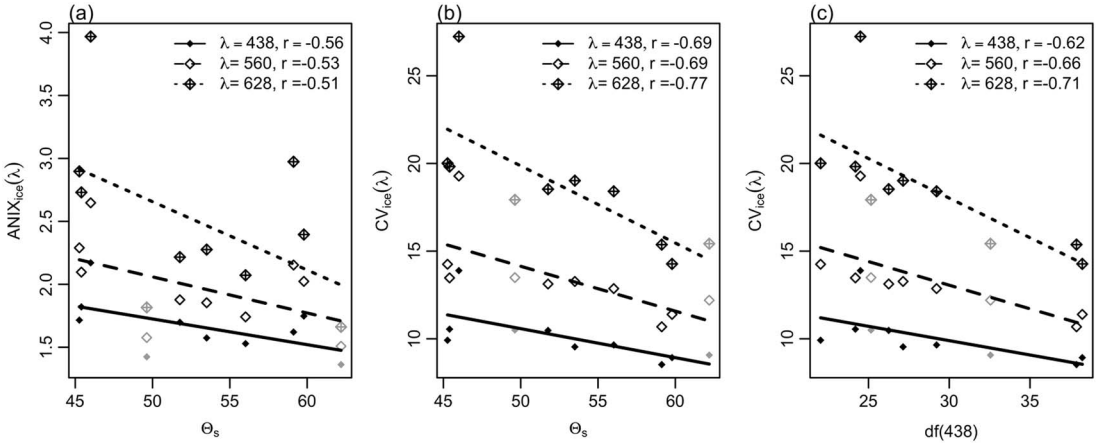

Figure 9. Variations in (a) ANIX(λ) and (b) CV(λ) with θ_s and between CV(λ) with df(438) (c) at 438, 560, and 628 nm for the selected bare ice surfaces when measured with the ASD (dark grey) and the CE600 (black). Lines indicate linear regressions per wavelength including ASD and CE600 data.

diffuse illumination with wavelength (e.g., Ball et al., 2015; Bourgeois et al., 2006; Dumont et al., 2009; Hudson et al., 2006; Perovich, 1994). However, wavelength dependency needs to be better quantified, particularly if we want to reconstruct hyperspectral reflectance data from the multispectral CE600 measurements. Therefore, wavelength dependency is further evaluated here as described in section 3.2 using (1) correlation coefficients to determine how much redundancy exists between channels, (2) the standard normal variate of the data to examine the shape of the reflectance spectra as a function of θ_v, θ_s, and $\Delta\phi$, and (3) a linear regression model to reconstruct the CE600 HDRF(λ) estimations at any wavelength.

Correlation matrices were computed between each wavelength pair of the HDRF(λ) data at each ASD station. Each pair presents 25 observations (i.e., 25 measurement angles). Patterns in correlation matrices are similar

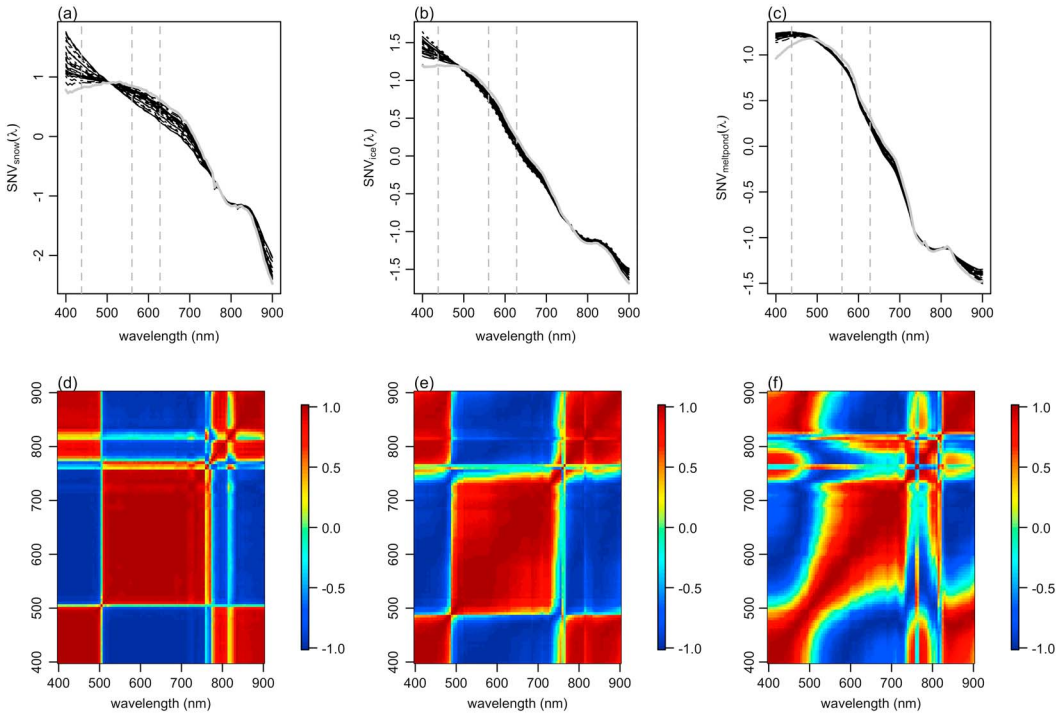

Figure 10. SNV(λ) spectra of HDRF(λ) estimations for the different viewing and illumination conditions and SNV correlation matrices between wavelength pairs for the snow (a and d, ASD53snow), bare ice (b and e, ASD63ice), and ponded ice (c and f, ASD50meltpond) surfaces measured with the ASD. Grey lines in Figures 10a–10c are the spectra at nadir.

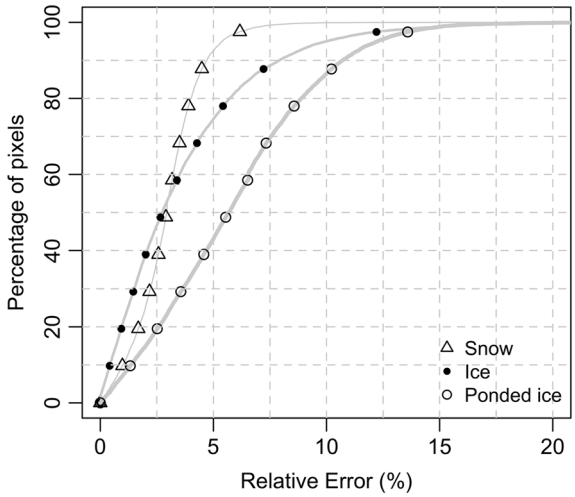

Figure 11. Percentage of pixels for different relative errors between the measured and regression-based HDRF(628) for three surfaces, bare ice (CE60060ice), snow (CE60056snow), and ponded ice (CE60056meltpond).

for all stations with correlation coefficients ranging between 0.92 and 1. Hence, HDRF(λ) measurements at all wavelengths appear highly correlated regardless of the surface type.

Figures 10a–10c show the SNV(λ) spectra corresponding to the snow, bare ice, and ponded ice surfaces shown in Figure 5. It reflects the shape of the spectra rather than the magnitude. Figures 10d–10f show the correlation matrices computed based on the SNV(λ) data in Figures 10a–10c. Hence, while the correlation coefficients computed on HDRF(λ) indicated that an increase in any spectral band leads to an increase in any other spectral band, the correlation matrix on SNV(λ) shows that the rate of increase is wavelength dependent. Several wavelength clusters of highly correlated SVN(λ) data are observed in Figures 10d–10f. Aside from the water absorption bands (i.e., near 750 and 820 nm), where correlations in SVN(λ) change rapidly with wavelength, we can distinguish two highly correlated band clusters. A first cluster includes the blue and NIR bands. A second cluster includes the green and red bands. Both clusters are negatively correlated with each other. Accordingly, the HDRF(λ) values may be reproduced for the entire 400–900 nm spectral range provided that the directional reflectance is given for at least one spectral band in each wavelength cluster (i.e., blue NIR and red-green). To verify this assumption, a regression analysis was conducted to evaluate HDRF(λ) in the red spectral region based on the blue and green HDRF(λ) estimations. Here a ridge regression is preferred to avoid imperfections in the regression analysis due to the high correlation between the different spectral bands (Hoerl & Kennar, 1970). The first step in the ridge regression is to standardize the dependent and independent variables. In other words, the regression analysis is performed on SNV(λ) estimations. Modeled data are then rescaled to the original scale to provide HDRF(λ) estimations. The modeled HDRF data at 628 nm are estimated as follows:

$$\mathrm{HDRF}_{\mathrm{RR}}(628) = C_{438}\mathrm{HDRF}(438) + C_{560}\mathrm{HDRF}(560) \tag{9}$$

where C_{438} and C_{560} are the ridge regression coefficients at 438 and 560 nm, respectively. These regression coefficients are estimated based on the SNV(λ) data derived from the ASD measurements and are then rescaled to the original scale, that is, HDRF(λ). For each surface the HDRF(λ) values from CE600 at 438 and 560 nm are used to predict the HDRF(λ) at 628 nm based on coefficients derived from ASD.

Figure 11 shows the RE estimated between the HDRF(λ) data measured with the CE600 camera and the regression based HDRF(λ) data at 628 nm for the bare ice, snow, and ponded ice surfaces shown in Figure 6. Relative errors remain relatively small particularly for the snow surfaces where 90% of the CE600 pixels shows errors below 5%. For the bare ice and ponded ice surfaces, relative errors remain below 10% for 90% of the pixels.

Observations are similar for all other stations. Note also that no particular spatial patterns in the relative error are observed for any surface type (not shown here). Hence, errors are not associated to particular viewing directions and the entire spectral shape can be reproduced provided that (1) regression coefficients are estimated a priori with hyperspectral observations and (2) that HDRF(λ) measurements are available for at least one spectral band in each wavelength cluster.

5. Conclusion

The present paper confirms the potential of the CE600 to measure commensurable HDRF(λ) values for ice and snow surfaces. It measures the radiance over a full hemisphere at an angular resolution of about 1° for several bands in the visible spectral range. In addition, the CE600 measurements present some substantial complementaries regarding to the ASD instrument. First, the measurement setup enables the estimation of the anisotropy of the reflectance at a large range of spatial resolutions from the composite scenes to the pixels. Accordingly, for comparison with spaceborne observations there is no need for scaling up the measurements from scene element to coarser earth surfaces. Moreover, the reflectance anisotropy gained in accuracy with the CE600 providing a higher range in directional reflectance over the surface. The hyperangular property of the CE600 allows measuring extrema in HDRF(λ) and particular features (e.g., darkening at grazing angles) that are overlooked with the ASD due to the limited number of measurement angles. The angular resolution affects

therefore the conclusions made about the anisotropy of the reflectance. Here we found that the coefficient of variation was less affected by the angular resolution relative to the anisotropy index (i.e., the ratio of the maximum to the minimum directional reflectance) often used in the literature to describe the extent in the anistropy of the reflectance.

One of the difficulties that arises when measuring HDRF(λ) with the CE600 camera is the spatial heterogeneity of the surface. Therefore, to ensure accurate CE600 measurements, a substantial number of images need to be taken over the same surface and averaged to smooth out artifacts related to surface irregularities (e.g., surface roughness and snow patches). In addition, shadow from the instrument and camera holders need to be extracted from the image. Several images are required to fill the gaps in surface radiance. Here HDRF(λ) values were estimated for snow and ice surfaces ranging from 1 m^2 to 80 m^2 with at least 20 valuable radiance images per surface and per wavelength. The minimum number of images should be chosen according to the surface type and the spatial variability observed over each surface. We found that the coefficient of variation estimated for each pixel represents a good approximation to quantify this variability.

Evaluation of illumination dependency of HDRF(λ) confirmed the need for a standard and accurate description of the illumination conditions without which field HDRF(λ) data comparison remains challenging. Additional information about the illumination conditions are essential, namely, the fraction of diffuse and direct illumination. This information is often missing in the studies encountered in the literature. A possible asset of the fish-eye camera is the direct measurement of incident light and subsequent surface albedo. Incident light may be measured by taking hemispheric sky images with the camera. This will allow an exact record of the sky and cloud conditions. In addition, it will eliminate the need for multiple instruments in the field and subsequent inaccuracies related to differences in angular and spectral responses. This should be considered in future work.

Evaluation of wavelength dependency of HDRF(λ) showed that patterns in HDRF(λ) for snow, bare ice, and ponded ice surfaces are very similar whatever the considered spectral band. This means that if the surface reflectance at a given wavelength λ is observed to increase/decrease in a given direction (e.g., in the direction of the specular reflection), we may expect that the surface reflectance will increase/decrease at all wavelengths in this particular direction. However, we observed that the rate of increase/decrease is wavelength dependent. We further investigated this based on SNV(λ) estimations. Correlations between SNV(λ) estimations allowed us to define wavelength clusters with highly correlated wavelength pairs. For the snow and ice surfaces, we defined a first cluster with the blue and NIR bands and a second cluster with the green and red bands. According to our results, based on a regression analysis, the entire spectral shape can be reproduced provided that regression coefficients are estimated a priori with hyperspectral observations and that HDRF(λ) measurements are available for at least one spectral band in each wavelength cluster. By combining the ASD and CE600 measurements, we are thus able to construct a hyperangular and hyperspectral snow and ice reflectance anisotropy data set. To our knowledge, such a data set is missing in the literature and highly valuable for, among other purposes, improving radiative transfer simulations. In a future work, this data will be used to provide sea ice and snow directional reflectance data for the simulation of top-of-atmosphere reflectance data at the vicinity of the ice edge with a three-dimensional radiative transfer model (Cornet et al., 2010). The spectral, angular, and spatial resolutions of the field directional reflectance data are critical to achieve comparability with airborne and satellite measurements. Therefore, the hyperangular and hyperspectral property of the present data set will enable the simulation of any narrow and broadband sensor measured signal at any viewing angle in the visible spectral range. The spatial resolution of the measurements will allow comparison with the surface field of view of the sensor or assist the scaling-up of the directional reflectance data from the field to the satellite.

Acknowledgments
We wish to acknowledge the anonymous reviewers for their constructive comments and helpful suggestions. Special thanks goes to Pierre Larouche for having graciously provided the ASD instrument and Don Perovich his metal arch for the ASD setup. This work was funded by ESA through the ESA Living Planet Fellowship Program and carried out in the frame of the GreenEdge project. We would also like to thank Debbie Christiansen-Stowe for reading our manuscript, Virginie Galindo and Margaux Gourdal for measuring the sea ice thickness and snow depth, and Gauthier Verin for sharing his snow specific surface area measurements. All data mentioned in the present paper will be made available through the GreenEdge data repository, http://www.greenedgeproject.info/data.php. The GreenEdge project is funded by the following French and Canadian programs and agencies: ANR (contract 111112), CNES (project 131425), IPEV (project 1164), CSA, Fondation Total, ArcticNet, LEFE, and the French Arctic Initiative (GreenEdge project). This project would not have been possible without the support of the Hamlet of Qikiqtarjuaq and the members of the community as well as the Inuksuit School and its Principal Jacqueline Arsenault. The project is conducted under the scientific coordination of the Canada Excellence Research Chair on Remote sensing of Canada's new Arctic frontier and the CNRS and Université Laval Takuvik Joint International Laboratory (UMI3376). The field campaign was successful thanks to the contribution of J. Ferland, G. Bécu, C. Marec, J. Lagunas, F. Bruyant, J. Lariviére, E. Rehm, S. Lambert-Girard, C. Aubry, C. Lalande, A. LeBaron, C. Marty, J. Sansoulet, D. Christiansen-Stowe, A. Wells, M. Benoît-Gagné, E. Devred, and M.-H. Forget from the Takuvik laboratory, C.J. Mundy and V. Galindo from University of Manitoba, and F. Pinczon du Sel and E. Brossier from Vagabond. We also thank Michel Gosselin, Québec-Océan, the CCGS Amundsen, and the Polar Continental Shelf Program for their in-kind contribution in polar logistic and scientific equipment.

References

Antoine, D., Morel, A., Leymarie, E., Houyou, A., Gentili, B., Victori, S., … Henry, P. (2013). Underwater radiance distributions measured with minitiaturized multispectral radiance cameras. *Journal of Atmospheric and Oceanic Technology*, *30*, 74–95.

Arnold, G. T., Tsay, S.-C., King, M. D., Li, J. Y., & Soulen, P. F. (2002). Airborne spectral measurements of surface-atmosphere anisotropy for arctic sea ice and tundra. *International Journal of Remote Sensing*, *23*(18), 3763–3781.

Ball, C. P., Marks, A. A., Green, P. D., MacArthur, A., Maturilli, M., Fox, N. P., & King, M. D. (2015). Hemispherical-Directional Reflectance (HDRF) of windowblown snow-covered Arctic tundra at large solar zenith angles. *IEEE Transactions on Geoscience and Remote Sensing*, *53*(10), 5377–5387.

Barnes, R. J., Dhanoa, M. S., & Lister, S. J. (1989). Standard normal variate transformation and de-trending of near infrared diffuse reflectance spectra. *Applied Spectroscopy*, *43*, 772–777.

Bourgeois, C. S., Calanca, P., & Ohmura, A. (2006). A field study of the hemispherical directional reflectance factor and spectral albedo of dry snow. *Journal of Geophysical Research*, *111*, D20108. https://doi.org/10.1029/2006JD007296

Cornet, C., Labonnote, L., & Szczap, F. (2010). Three-dimensional polarized monte-carlo atmospheric radiative transfer model (3DMCPOL): Effects on polarized visible reflectances of a cirrus cloud. *Journal of Quantitative Spectroscopy and Radiative Transfer*, *111*, 174–186.

Doctor, K. Z., Bachmann, C. M., Gray, D. J., Montes, M. J., & Fusina, R. A. (2015). Wavelength dependence of the bidirectional reflectance distribution (BRDF) of beach sands. *Applied Optics*, *54*(31), 243–255.

Dumont, M., Brissaud, O., Picard, G., Schmitt, B., Gallet, J.-C., & Arnaud, Y. (2009). High accuracy measurements of snow Bidirectional Reflectance Distribution Function at visible and NIR wavelengths—Comparion with modelling results. *Atmospheric Chimestry and Physics Discussion*, *9*, 19,279–19,311.

Dymond, J. R., & Trotter, C. M. (1997). Directional reflectance of vegetation measure by a calibrated digital camera. *Applied Optics*, *36*, 4314–4318.

Ehrlich, A., Bierwirdth, E., Wendisch, M., Herber, A., & Gayet, J.-F. (2012). Airborne hyperspectral observations of surface and cloud directonal reflectivity using a commercial digital camera. *Atmospheric Chemistry and Physics*, *12*, 3493–3510.

Gallet, J. C., Domine, F., & Dumont, M. (2014). Measuring the specific surface area of wet snow using 1310 nm reflectance. *The Cryosphere*, *8*, 1139–1148.

Gregg, W., & Carder, K. (1990). A simple spectral solar irradiance model for cloudless maritime atmospheres. *Limnology and Oceanography*, *35*, 1657–1675.

Grenfell, T. C., & Perovich, D. K. (2004). Seasonal and spatial evolution of albedo in a snow-ice-land-ocean environment. *Journal of Geophyiscal Research*, *109*, C01001. https://doi.org/10.1029/2003JC001866

Hoerl, A. E., & Kennar, R. W. (1970). Ridge regression: Biased estimation for non orthogonal problems. *Technometrics*, *12*(3), 55–67.

Hudson, S., Warren, S., Brandt, R., Grenfell, T., & Six, D. (2006). Spectral bidirectional reflectance of Antarctic snow: Measurements and parameterization. *Journal of Geophysical Research*, *111*, D20108. https://doi.org/10.1029/2006JD007290

International Ocean-Colour Coordinating Group (2016). Ocean color remote sensing in polar seas. In *Reports of the International Ocean-Colour Coordinating Group, IOCCG*.

Li, S., & Zhou, X. (2004). Modelling and measuring the spectral bidirectional reflectance factor of snow-covered sea ice: An intercomparison study. *Hydrological processes*, *18*, 3559–3581.

Marks, A., Fragiacomo, C., MacArthur, A., Zibordi, G., Fox, N., & King, M. D. (2015). Characterisation of the HDRF (as a proxy for BRDF) of snow surfaces at Dome C, Antarctica, for the inter-calibration and inter-comparison of satellite optical data. *Remote Sensing of Environment*, *158*(1), 407–416.

Milton, E. J., Schaepman, M. E., Anderson, K., Kneubuhler, M., & Fox, N. (2009). Progress in field spectroscopy. *Remote Sensing of Environment*, *113*, 92–109.

Nandy, P., Thome, K., & Biggar, S. (1998). Instrument for retrieval of BRDF data for vicarious calibration. *IEEE International Geoscience and Remote Sensing Symposium Proceedings (1998)*, *2*, 562–564.

Nandy, P., Thome, K., & Biggar, S. (2001). Characterization and field use of a CCD camera system for retrieval of bi-directional reflectance distribution function. *Journal of Geophysical Research*, *101*, 11,975–11,966.

Nicodemus, F. E. (1965). Directional reflectance and emissivity of an opaque surface. *Applied Optics*, *4*, 767–775.

Nicodemus, F. E., Richemond, J. C., Hsia, J. J., Ginsberg, I. W., & Limperis, T. (1977). *Geometrical considerations and nomenclature for reflectance*. Washington, DC: National Bureau of Standards, US Department of Commerce. Retrieved from http://physics.nist.gov/Divisions/Div844/facilities/specphoto/pdf/geoConsid.pdf

Painter, T., & Dozier, J. (2004). Measurements of the hemispherical-directional reflectance of snow at fine spectral and angular resolution. *Journal of Geophysical Research*, *109*, D18115. https://doi.org/10.1029/2003JD004458

Perovich, D. K. (1994). Light reflectance from sea ice during the onset of melt. *Journal of Geophysical Research*, *99*(C2), 3351–3359.

Sandmeier, S., Muller, C., Hosgood, B., & Andreoli, G. (1998). Physical mechanisms in hyperspectral BRDF data of grass and watercress. *Remote Sensing of Environment*, *66*, 222–233.

Schaepman-Strub, G., Schaepman, M., Painter, T., Dangel, S., & Martonchik, J. (2006). Reflectance quantities in optical remote sensing—Defintions and case studies. *Remote Sensing of Environment*, *103*, 27–42.

Tanre, D., Herman, M., & Deschamps, P. Y. (1983). Influence of the atmosphere on space measurements of directional properties. *Applied Optics*, *22*, 733–741.

Taylor, V. R., & Stowe, L. L. (1984). Reflectance characteristics of uniform earth and cloud surfaces derived from NIMBUS-7 ERB. *Journal of Geophysical Research*, *89*(4), 4987–4996.

Vermote, E. F., & Vermuelen, A. (1999). Atmospheric correction algorithm: Spectral reflectance (MOD09). In *MODIS ATBD Version 4.0 NAS5-96062*.

Warren, S. G. (1982). Optical properties of snow. *Reviews of Geophysics and Space Physics*, *20*(1), 67–89.

Yackel, J. J., Barber, D. G., Papakyriakou, T. N., & Breneman, C. (2007). First-year sea ice spring melt transitions in the Canadian Arctic Archipelago from time-series synthetic aperture radar data, 1992–2002. *Hydrological Processes*, *21*, 253–265.